

## Phase behavior of a simple fluid confined between chemically corrugated substrates

Henry Bock\*

*Institut für Theoretische Physik, Sekretariat PN 7-1, Fachbereich Physik, Technische Universität Berlin, Hardenbergstraße 36, D-10623 Berlin, Germany*

Martin Schoen†

*Fachbereich Physik, Bergische Universität Wuppertal, Gaußstraße 20, D-42097 Wuppertal, Germany*

(Received 14 July 1998)

The phase behavior of a molecularly thin fluid film of Lennard-Jones (LJ)(12,6) fluid confined to a chemically heterogeneous slit-shaped pore was investigated by the grand canonical ensemble Monte Carlo (GCEMC) method. The slit-shaped pore comprises two identical plane-parallel solid substrates, each of which consists of alternating strips of LJ(12,6) solid of two types: strongly (width  $d_s$ ) and weakly adsorbing (width  $d_w$ ). With the substrates aligned so that strips of the same type oppose each other, GCEMC was used to compute the local and mean densities of the fluid as well as its isothermal compressibility as functions of substrate separation  $s_z$  and for various degrees of chemical corrugation measured quantitatively in terms of  $c_r := d_s / (d_s + d_w)$ . Depending on  $s_z$  and  $c_r$ , the confined fluid may consist of inhomogeneous gaslike or liquidlike phases filling the entire volume between the substrates. In addition, liquid “bridges” may form as a third phase consisting of stratified liquid stabilized by the “strong” strips and separated from two surrounding gaslike regions by an interface. The phase diagram involving all three phases was determined for a mean-field lattice-gas model similar to the one investigated recently by Röcken and Tarazona [J. Chem. Phys. **105**, 2034 (1996)]. The lattice-gas calculations permit a qualitative interpretation of the complex dependence of the GCEMC results on both  $s_z$  and  $c_r$ . [S1063-651X(99)07704-1]

PACS number(s): 61.20.Ja, 61.20.Ne, 68.45.-v, 64.70.Fx

### I. INTRODUCTION

In many areas of contemporary science and technology, one is confronted with the problem of miniaturizing parts of the system of interest in order to control processes on very short length and time scales [1]. For example, to study the kinetics of certain chemical reactions, reactants have to be mixed at a sufficiently high speed. By miniaturizing a continuous-flow mixer, Knight *et al.* recently showed that nanoliters can be mixed within microseconds, thus permitting one to study fast reaction kinetics on time scales unattainable with conventional mixing technology [2]. The importance to design and construct microscopic machines gave rise to a new field in applied science and engineering known as “microfabrication technology” or “microengineering” [3]. One of the key problems in microengineering consists of the fabrication of chemical or geometrical structures on a nanometer to micrometer length scale with high precision. This can nowadays be accomplished by a variety of techniques. For example, by means of various lithographic methods [3,4] or wet chemical etching [5], the surfaces of solid substrates can be endowed with well-defined nanoscopic lateral structures. In yet another method the substrate is chemically patterned by elastomer stamps, and, in certain cases, subsequent chemical etching [6–9].

In this paper we focus on substrates with prescribed chemical heterogeneities [10,11]. One realization of such substrates is the so-called “Janus bead,” which is a spherical

colloidal particle with one hemisphere hydrophilic, the other one being hydrophobic [12,13]. Along the equator the two portions of the substrate have a rather sharp and well-defined junction. Janus beads can be considered as amphiphilic solids with a stabilizing effect on oil-water interfaces [12].

Theoretically there has also been considerable interest in fluids near chemically heterogeneous substrates in recent times. For example, Koch, Dietrich, and Napiórkowski [14] considered a fluid adsorbed on a single planar substrate consisting of two semi-infinite parts, only one of which is wetted by the fluid. They showed that for large distances from the junction between the two portions of the substrate, the density profile of the fluid corresponds to that over a chemically *homogeneous* substrate composed of either material. However, the precise range over which the presence of the junction affects the density profile in the transverse directions (i.e., parallel to the substrate surface) is not yet known quantitatively [15]. For substrate materials with various chemical patterns, Lenz and Lipowsky [16] studied the morphology and phase behavior of droplets with typical sizes on a micrometer length scale where neither gravity nor van der Waals forces are relevant.

While all these studies are concerned with fluids near single chemically heterogeneous substrates, interesting effects are to be expected if a fluid phase is confined by such substrates to spaces of microscopic or mesoscopic dimensions. Even if the substrate is composed of just a single chemical species, the phase behavior of a confined fluid differs markedly from that of a corresponding bulk fluid [17]. Perhaps the most prominent aspect in this regard concerns the location of the critical point which is shifted to lower temperature and higher mean density compared with its bulk

\*Electronic address: henry@ozon.physik.tu-berlin.de

†Electronic address: schoen@wpta9.physik.uni-wuppertal.de

counterpart (see Fig. 7 in Ref. [18]). Unlike in the bulk the critical point of a confined fluid is not unique but depends on the degree of confinement; that is, the critical-point shift decreases with substrate separation. Critical-point shifts in confined fluids have extensively been studied both experimentally [18–24] and theoretically [25–32].

If the substrate material is chemically heterogeneous, it is conceivable that the phase behavior of confined fluids is even richer because chemical corrugation of the substrate is superimposed on confinement effects. For example, for chemically striped substrate materials—that is, substrates consisting of strongly adsorbing portions alternating with weakly adsorbing ones in one transverse dimension—the chemical heterogeneity can engender phase coexistence. For a fluid confined between two planar, parallel, and chemically striped substrates, as was shown in Ref. [33], a gas over the weakly attractive portions of the opposite substrates can be in thermodynamic equilibrium with a liquid over the strongly adsorbing ones. The two are separated by an interface that can be described by a semiempirical model usually applied to the density variation across a liquid-gas interface in the bulk [34]. “Internal” phase coexistence of this sort was also investigated by Röcken and Tarazona [35], who studied capillary condensation in slit-shaped pores with chemically corrugated walls using a mean-field lattice-gas model. In their model the wall is represented by a potential field that oscillates sinusoidally between attraction and repulsion in one transverse direction ( $x$ ), and extends about one molecular diameter from the plane of the wall. For a single substrate separation Röcken and Tarazona investigated the effect of substrate corrugation (i.e., the period of oscillation between attraction and repulsion) on the phase diagram of the confined fluid. More recently, Röcken *et al.* employed density functional calculations to investigate the phase behavior of more realistic model fluids confined between chemically corrugated substrates [36].

In this paper we are concerned with variations of the degree of chemical corrugation of the substrate material, that is, with variations of the relative widths of strongly and weakly adsorbing portions of chemically striped substrates in a spirit similar to Röcken and co-workers’ work [35,36]. However, unlike these authors we also study the phase behavior of confined fluids as a function of distance  $s_z$  between the substrates. We employ grand canonical ensemble Monte Carlo (GCEMC) simulations, in which the thermodynamic state of the fluid is characterized by the chemical potential  $\mu$  and temperature  $T$  (as well as other natural variables of the grand potential  $\Omega$ , see Ref. [37]). To interpret the GCEMC results, we employ a mean-field lattice-gas model similar to the one studied by Röcken and Tarazona [35]. However, our model differs from that of Ref. [35] by a different fluid-substrate interaction potential which is motivated by the one employed in the parallel computer simulations. Varying  $s_z$  under conditions of fixed  $\mu$  and  $T$  resembles operating conditions of the surface forces apparatus (SFA) [38]. The results of this work should therefore be amenable (at least in principle) to direct experimental verification in a qualitative sense.

The remainder of the paper is organized as follows. In Sec. II we describe the model system employed in the computer simulations. Results of these simulations are also presented in Sec. II. In Sec. III we introduce the mean-field

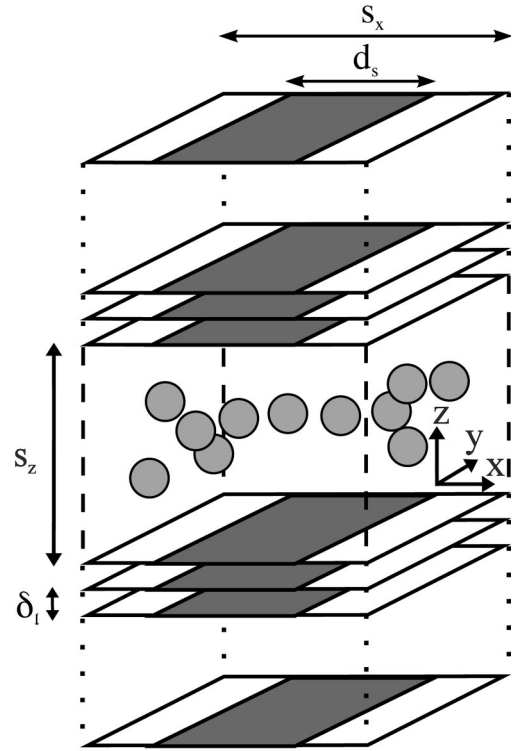


FIG. 1. Scheme of a simple fluid confined by a chemically heterogeneous model pore. Fluid molecules (gray spheres) are spherically symmetric. Each substrate consists of a sequence of crystallographic planes separated by a distance  $\delta_s$  along the  $z$  axis. The surface planes of the two opposite substrates are separated by a distance  $s_z$ . Periodic boundary conditions are imposed in the  $x$  and  $y$  directions (see text).

model, and compare it with the simulation results. Our findings are summarized in Sec. IV.

## II. GRAND CANONICAL ENSEMBLE MONTE CARLO SIMULATIONS

### A. Model system

Our model system, sketched in Fig. 1, consists of a fluid composed of spherically symmetric molecules which is sandwiched between the surfaces of two solid substrates. The substrate surfaces are planar, parallel, and separated by a distance  $s_z$  along the  $z$  axis of the coordinate system. The substrates are semi-infinite in the  $z$  direction, occupying the half spaces  $s_z/2 \leq z < \infty$  and  $-\infty < z \leq -s_z/2$ , and are infinite in the  $x$  and  $y$  directions. Each substrate comprises alternating slabs of two types: strongly adsorbing and weakly adsorbing. The “strong” and “weak” slabs have widths  $d_s$  and  $d_w$ , respectively, in the  $x$  direction, and are infinite in the  $y$  direction. The system is thus periodic in the  $x$  direction of period  $d_s + d_w$  and is translationally invariant in the  $y$  direction. In practice we take the system to be a finite piece of the fluid, imposing periodic boundary conditions [39] on the planes  $x = \pm s_x/2$  and  $y = \pm s_y/2$ .

The substrates are in registry in that slabs of the same type are exactly opposite each other. Substrate atoms are assumed to be of the same “diameter” ( $\sigma$ ) and to occupy the sites of the fcc lattice [the substrate surfaces are taken to be (100) planes] having lattice constant  $\ell$ , which is taken to

be the same for both species. Thus substrate species are distinguished only by the strength of their interaction with fluid molecules. We assume the total potential energy to be a sum of pairwise additive Lennard-Jones (LJ)(12,6) potentials, all of which have the form

$$u(r) = 4\epsilon \left[ \left( \frac{\sigma}{r} \right)^{12} - \left( \frac{\sigma}{r} \right)^6 \right], \quad (1)$$

where  $\epsilon$  is the well depth,  $\sigma$  the molecular ‘‘diameter,’’ and  $r$  the distance between the centers of a pair of particles (i.e., fluid molecules or substrate atoms). For the interaction between a pair of fluid molecules,  $\epsilon = \epsilon_{ff}$  [i.e.,  $u_{ff}(r)$ ]. The nanoscale heterogeneity of the substrate is characterized by

$\epsilon = \epsilon_{fs}$  [i.e.,  $u_{fs}(r)$ ] for the interaction of a fluid molecule with a substrate atom in the strong (central) slab, and by  $\epsilon = \epsilon_{fw}$  [i.e.,  $u_{fw}(r)$ ] for the interaction of a fluid molecule with a substrate atom in either of the two weak (outer) slabs (see Fig. 1). We take  $\epsilon_{fs} > \epsilon_{ff}$  and  $\epsilon_{fw} \ll \epsilon_{ff}$  (see Sec. II B) for specific values).

Since we are concerned with the effects of chemical heterogeneity at the nanoscale on the behavior of the confined fluid, we expect details of the atomic structure not to matter greatly. Therefore, we adopt a mean-field representation of the interaction of a fluid molecule with the substrate, which we obtain by averaging the fluid-substrate interaction potential over positions of substrate atoms in the  $x$ - $y$  plane. The resulting mean-field potential can be expressed as [33]

$$\Phi^{[k]}(x, z; s_x, s_z) = \frac{2}{\ell^2} \sum_{m=-\infty}^{\infty} \sum_{m'=0}^{\infty} \int_{-\infty}^{\infty} dy' \left\{ \int_{-s_x/2+ms_x}^{-d_s/2+ms_x} dx' u_{fw}(|\mathbf{r}-\mathbf{r}'|) + \int_{-d_s/2+ms_x}^{d_s/2+ms_x} dx' u_{fs}(|\mathbf{r}-\mathbf{r}'|) + \int_{d_s/2+ms_x}^{s_x/2+ms_x} dx' u_{fw}(|\mathbf{r}-\mathbf{r}'|) \right\}. \quad (2)$$

In Eq. (2),  $2/\ell^2$  is the areal density of the (100) plane of the fcc lattice. The position of a fluid molecule is denoted by  $\mathbf{r}$ , and  $\mathbf{r}' = (x', y', z' = \pm s_z/2 \pm m' \delta_\rho)$  represents the position of a substrate atom, where ‘‘-’’ refers to the lower ( $k=1$ ) substrate, ‘‘+’’ refers to the upper ( $k=2$ ) substrate, and  $\delta_\rho$  is the spacing between successive crystallographic planes in the  $\pm z$  direction. As detailed in Ref. [33], one eventually obtains

$$\begin{aligned} \Phi^{[k]} = & -3\pi \left( \frac{\sigma}{\ell} \right)^2 \sum_{m=-\infty}^{\infty} \sum_{m'=0}^{\infty} \left\{ (\epsilon_{fw} - \epsilon_{fs}) \Delta \left( x + \frac{d_s}{2} - ms_x, \frac{s_z}{2} + m' \delta_\rho \pm z \right) \right. \\ & - (\epsilon_{fw} - \epsilon_{fs}) \Delta \left( x - \frac{d_s}{2} - ms_x, \frac{s_z}{2} + m' \delta_\rho \pm z \right) \\ & \left. - \epsilon_{fw} \left[ \Delta \left( x + \frac{s_x}{2} - ms_x, \frac{s_z}{2} + m' \delta_\rho \pm z \right) - \Delta \left( x - \frac{s_x}{2} - ms_x, \frac{s_z}{2} + m' \delta_\rho \pm z \right) \right] \right\} \end{aligned} \quad (3)$$

from Eq. (2), where the sign on  $z$  is chosen according to the convention  $+\leftrightarrow k=1$  and  $-\leftrightarrow k=2$  (see Fig. 1). In Eq. (3), the auxiliary function  $\Delta$  is defined as

$$\Delta(x'', z'') := \frac{21}{32} I_3(x'', z'') - I_4(x'', z''), \quad (4)$$

where

$$I_3(x'', z'') = \frac{x'' \sigma^{10}}{9z''^2 \sqrt{R^9}} \left[ 1 + \frac{8}{7} S + \frac{48}{35} S^2 + \frac{64}{35} S^3 + \frac{128}{35} S^4 \right] \quad (5)$$

and

$$I_4(x'', z'') = \frac{x'' \sigma^4}{3z''^2 \sqrt{R^3}} [1 + 2S]. \quad (6)$$

In Eqs. (5) and (6), we also introduced  $R := x''^2 + z''^2$  and  $S := R/x''^2$ . For symmetry reasons  $\Phi^{[k]}$  needs only be represented in one quadrant (say,  $0 \leq x \leq s_x/2$ ,  $0 \leq z \leq s_z/2$ ) of the  $x$ - $z$  plane [33]. In this quadrant  $\Phi^{[k]}$  is computed at the

nodes of a two-dimensional grid prior to the simulation where we employ a mesh of  $\delta_x = \delta_z = 0.025\sigma$ . In practice, a sufficiently accurate numerical representation of  $\Phi^{[k]}$  is obtained by replacing the double sum in Eq. (3) by  $\sum_{m=-2}^{m=2} \sum_{m'=0}^{m'=50} \dots$ , as tests in Ref. [33] revealed. During the simulation the value of  $\Phi^{[k]}$  corresponding to the actual position of a fluid molecule is computed by two-dimensional interpolation between the nodes, as detailed in Ref. [33].

## B. Microscopic structure and phase behavior

In the remainder of Sec. II, numerical values are given in dimensionless units based on the parameters of the LJ(12,6) potential for the fluid-fluid interaction: distance is given in units of  $\sigma$ , energy in units of  $\epsilon_{ff}$ , and temperature in units of  $\epsilon_{ff} k_B^{-1}$ . We fix the substrate parameters  $\epsilon_{fw} = 0.001$ ,  $\epsilon_{fs} = 1.25$ , and  $d_s = 4.0$ . We also fix  $T = 1.00$  and  $\mu = -11.50$ , for which the Lennard-Jonesium bulk phase is a gas with a(n average) number density  $\rho_b = \langle N \rangle / V = 0.036$ . The effect of chemical heterogeneity of the substrate is investigated by varying  $s_x$ ; that is, the width of the weakly attractive strip

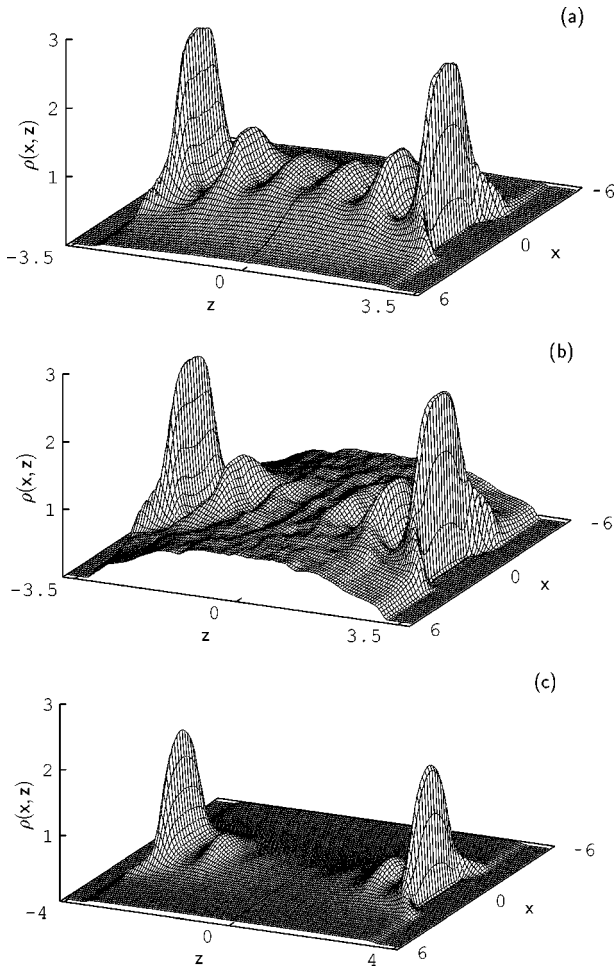


FIG. 2. Local density  $\rho(x, z)$  as a function of position in the  $x$ - $z$  plane for  $s_x = 12.0$ . (a)  $s_z = 7.2$ . (b)  $s_z = 7.5$ . (c)  $s_z = 8.2$ .

( $d_w$ ) since  $d_s$  remains constant. The distance between the substrates is varied over the range  $2.0 \leq s_z \leq 13$ .

### 1. Structure of confined fluids

The simplest quantitative measure of fluid structure in an inhomogeneous system is the local density defined as

$$\rho(x, z) = \frac{\langle N(x, z) \rangle}{\Delta x \Delta z s_y}, \quad (7)$$

which is a function of  $x$  and  $z$  because of the chemically heterogeneous nature of the substrate. In Eq. (7),  $N(x, z)$  is the number of fluid molecules in a given configuration that are located in a square prism of dimensions  $\Delta x \times s_y \times \Delta z$  centered on a point  $(x, z)$ . In Fig. 2 we plot  $\rho(x, z)$  for three selected values of  $s_z$  and  $s_x = 12.0$ . Because of the symmetry of  $\Phi^{[k]}$ ,  $\rho(x, z)$  must be symmetric about the  $x=0$  and  $z=0$  planes (see Fig. 2). Peaks in  $\rho(x, z)$  represent positions of molecular strata. For  $s_z = 7.2$  a stratified “liquid” bridges the gap between the strongly attractive portions of the opposite substrates [i.e., for  $|x| \leq 2.0$ ; see Fig. 2(a)]. Because of the decay of the fluid-substrate interaction potential, stratification diminishes as  $z$  increases along lines of constant  $x$ . Stratification is absent over the weakly attractive portion of the substrate. Here an inhomogeneous gas exists, as indicated by the low value of  $\rho(x, z)$  and its weak dependence on

$x$  and  $z$  for  $|x| \geq 4.0$ . The interfacial region between the stratified portion of the fluid and the surrounding gas can be described by a semiempirical model usually applied to the liquid-gas interface in the bulk [34]. In the remainder of this paper, the term “liquid bridge (phase)” always refers to situations akin to the one depicted in Fig. 2(a): a stratified fluid stabilized by the strongly attractive part of the substrate plus a surrounding gas over the two outer, weakly attractive portions of the substrate material.

For larger  $s_z = 7.5$  [see Fig. 2(b)], the structure of the fluid changes significantly. Over the strongly attractive portion of the substrate, the fluid remains stratified. However, the gaslike phase has given way to an inhomogeneous liquidlike phase over the weakly attractive portion of the substrate. Consequently, the liquid-gas interface visible in Fig. 2(a) has disappeared, and can no longer be seen in Fig. 2(b). Since the weak portions of the substrate are essentially repulsive,  $\rho(x, z)$  decreases for  $|x| \geq 4.0$  from the center of the fluid ( $z=0$ ) toward the substrate ( $|z| \rightarrow s_z/2$ ).

If the distance between the substrates is increased even further, another significant structural change occurs in the fluid. It is illustrated by the plot of  $\rho(x, z)$  for  $s_z = 8.2$  in Fig. 2(c) where the fluid bridge disappeared and only two strata of fluid molecules “cling” to the strongly attractive portion of the substrate. For example, for  $|z| \leq 3$  and  $x=0$  the density is gaslike, and decreases monotonically toward the center of the fluid at  $z=0$ . The height of the two maxima of  $\rho(x, z)$  appears to be substantially reduced compared with the plots in Figs. 2(a) and 2(b). Thus by increasing  $s_z$  the liquidlike phase [see Fig. 2(b)] eventually evaporates, leaving behind two inhomogeneous fluid columns (because of the translational invariance of the density in the  $y$  direction) that are stabilized by the strongly attractive portions of the opposite substrates. These columns are surrounded by a gaslike phase of low density, as revealed by the plot in Fig. 2(c). The sequence of plots in Figs. 2(a)–2(c) illustrates the peculiar phase transition from a liquid bridge to a liquidlike phase and eventually to a gaslike phase with increasing  $s_z$  [33,34].

### 2. Variation of strip width

Since our focal point is the effect of chemical corrugation of the substrate on the phase behavior of the confined fluid, integral quantities like the mean pore density and its fluctuations are better suited for a systematic study than the local density analyzed in Sec. II B 1, because the latter conveys too much information. Fluctuations of the mean pore density are particularly sensitive to phase transitions [40], and can be cast quantitatively in terms of the isothermal compressibility. To derive a molecular expression for it we start from the Gibbs-Duhem relation [37]

$$0 = -SdT - Nd\mu + (T_{xx} - T_{yy})A_x ds_x + (T_{zz} - T_{yy})A_z ds_z - A_y d(s_y T_{yy}), \quad (8)$$

which follows from the exact differential of the grand potential  $\Omega$ ,

$$d\Omega = -SdT - Nd\mu + T_{xx}s_y s_z ds_x + T_{yy}s_x s_z ds_y + T_{zz}s_x s_y ds_z, \quad (9)$$

by noting that for fixed  $T$ ,  $\mu$ ,  $s_x$ , and  $s_z$ ,  $\Omega$  is a homogeneous function of degree one in  $s_y$ , so that Euler's theorem applies. Under these conditions the latter yields  $\Omega = T_{yy}V$ , where  $V = s_x s_y s_z$ . In Eq. (8),  $S$  is the entropy,  $N$  is the number of molecules accommodated by the fluid,  $A_\alpha$  is the area of the  $\alpha$ -directed face of the fluid, and  $T_{\alpha\alpha}$  ( $\alpha = x, y, z$ ) are diagonal elements of the stress tensor  $T$  [33]. For fixed  $T$ ,  $s_x$ , and  $s_z$  we have, from Eq. (8),

$$Nd\mu = -A_y d(s_y T_{yy}), \quad (10)$$

from which the definition of the isothermal compressibility  $\kappa_{yy}$ ,

$$N \left( \frac{\partial \mu}{\partial N} \right)_{T, s_x, s_y, s_z} = - \left( \frac{\partial (s_y A_y T_{yy})}{\partial N} \right)_{T, s_x, s_y, s_z} =: \frac{V}{N} \kappa_{yy}^{-1}, \quad (11)$$

follows after a few straightforward algebraic manipulations [33]. We deviate from standard notation to emphasize that the isothermal compressibility is related to the stress tensor element  $T_{yy}$  on account of the symmetry of the system. From Eq. (9), we have

$$\left( \frac{\partial \Omega}{\partial \mu} \right)_{T, s_x, s_y, s_z} = -N, \quad (12)$$

from which

$$\left( \frac{\partial^2 \Omega}{\partial \mu^2} \right)_{T, s_x, s_y, s_z} = - \left( \frac{\partial N}{\partial \mu} \right)_{T, s_x, s_y, s_z} \quad (13)$$

immediately follows.

The linkage to the molecular scale is provided by the well-known statistical thermodynamic relation [41]

$$\Omega(T, \mu, V) = -k_B T \ln \Xi(T, \mu, V), \quad (14)$$

where  $k_B$  is Boltzmann's constant, and

$$\Xi(T, \mu, s_x, s_y, s_z) = \sum_{N=0}^{\infty} \frac{\exp[\mu N / k_B T]}{N! \Lambda^{3N}} Z_N(T, s_x, s_y, s_z) \quad (15)$$

is the grand canonical partition function for a classical system in which the molecules possess only translational degrees of freedom. In Eq. (15),  $\Lambda$  denotes the thermal de Broglie wave length [42] and  $Z_N$  is the configurational integral. Combining Eqs. (11) and (13)–(15), we obtain

$$\kappa_{yy} = - \frac{V}{\langle N \rangle^2} \left( \frac{\partial^2 \Omega}{\partial \mu^2} \right)_{T, s_x, s_y, s_z} = \frac{V}{k_B T} \frac{\langle N^2 \rangle - \langle N \rangle^2}{\langle N \rangle^2} \quad (16)$$

as the desired molecular expression for  $\kappa_{yy}$ . Because of

$$\bar{\rho} := - \frac{1}{V} \left( \frac{\partial \Omega}{\partial \mu} \right)_{T, s_x, s_y, s_z} = \frac{\langle N \rangle}{V} = \frac{1}{A_y} \int_{-s_x/2}^{s_x/2} dx \int_{-s_z/2}^{s_z/2} dz \rho(x, z) \quad (17)$$

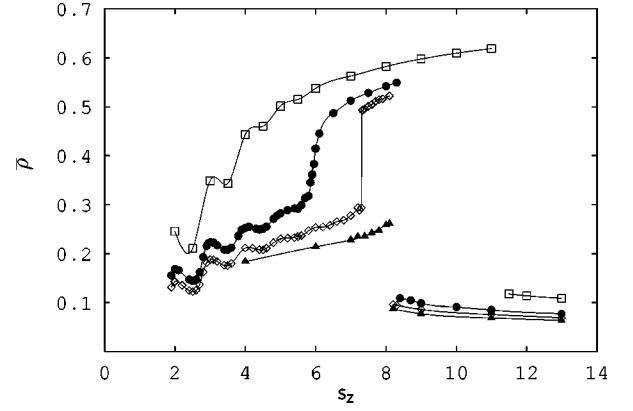


FIG. 3. Mean density  $\bar{\rho}$  as a function of substrate separation  $s_z$  and various degrees of chemical corrugation of substrate  $c_r = 4/7$  ( $\square$ ),  $c_r = 4/10$  ( $\bullet$ ),  $c_r = 4/12$  ( $\diamond$ ), and  $c_r = 4/14$  ( $\blacktriangle$ ). Solid lines are intended to guide the eye.

one expects the average fluid density to change discontinuously during a first-order phase transition, whereas this quantity varies continuously during a continuous phase transition. In this latter case  $\kappa_{yy}$  should diverge to infinity (see Sec. 6.4 in Ref. [43] and Sec. III D of this work). We note in passing that an expression like the one in Eq. (17) linking a local  $[\rho(x, z)]$  property to a global ( $\bar{\rho}$ ) fluid property does not exist as far as  $\kappa_{yy}$  is concerned.

Plots of  $\bar{\rho}$  versus  $s_z$  are shown in Fig. 3 for various degrees of chemical corrugation of the substrate quantitatively expressed in terms of  $c_r := d_s / (d_s + d_w) = d_s / s_x$ . For  $c_r = \frac{4}{7}$ ,  $\bar{\rho}$  oscillates for  $s_z \lesssim 6$  with a period of approximately one molecular ‘‘diameter.’’ A similar behavior of  $\bar{\rho}$  is found for  $c_r = \frac{4}{10}$  and  $\frac{4}{12}$ , which can be interpreted as a fingerprint of stratification [see Fig. 2(a)], that is the change in the number of molecular strata accommodated between the substrates with varying  $s_z$  [44,45].

However, in the limit  $s_z \rightarrow \infty$  the confined fluid becomes increasingly bulklike on account of the vanishing influence of fluid-substrate interactions. Because the bulk phase is a gas under the present conditions, one expects a first-order phase transition from denser confined phases at smaller  $s_z$  to a gaslike phase at some characteristic substrate separation. This transition, known as capillary condensation (evaporation), is, in fact, observed for  $c_r = \frac{4}{7}$  around  $s_z \approx 11.0$ . For  $c_r = \frac{4}{10}$ , capillary condensation shifts to smaller  $s_z \approx 8.3$ , which is reasonable in view of the reduced *net* strength of attractive fluid-substrate interactions compared with  $c_r = \frac{4}{7}$ . The shift of capillary condensation to lower substrate separation also persists for  $c_r = \frac{4}{12}$  and  $\frac{4}{14}$ , but is much less pronounced, as Fig. 3 reveals. However, comparing only the latter two, chemical corrugation of the substrate seems to be of marginal importance for the location of the first-order transition encountered upon reducing  $s_z$  from large values [where the confined fluid is an inhomogeneous gaslike phase; see Fig. 2(c)].

However, under favorable conditions more than just one first-order phase transition may occur. This is evident from the plot of  $\bar{\rho}$  for  $c_r = \frac{4}{12}$  where a second discontinuity is observed around  $s_z \approx 7.3$ . As we shall see below in Sec. III D, the second phase transition is a direct consequence of

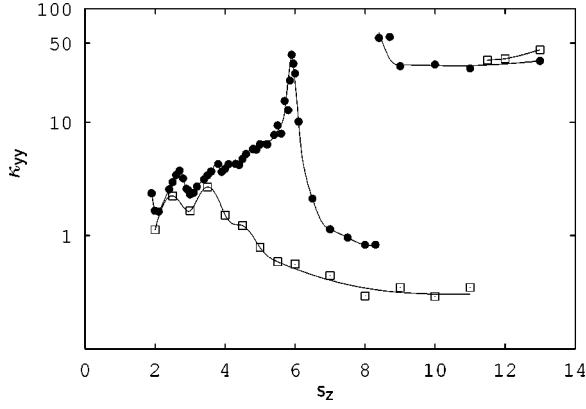


FIG. 4. As in Fig. 3, but for isothermal compressibility  $\kappa_{yy}$ ;  $c_r = 4/7$  ( $\square$ ) and  $c_r = 4/10$  ( $\bullet$ ).

the heterogeneous substrate. Similar multiple transitions have recently been reported for fluids confined by chemically homogeneous but nonplanar substrates [46].

For  $c_r = \frac{4}{10}$  this second discontinuity vanishes in favor of a rather steep increase of  $\bar{\rho}$  over the range  $5.5 < s_z < 6.5$ . A corresponding plot of  $\kappa_{yy}(s_z)$  in Fig. 4 has a tall, cusplike peak in the same range of substrate separations. In the vicinity of this peak  $\kappa_{yy}$  depends on the size of the simulation cell in the translationally invariant direction ( $y$ ). This indicates that the correlation length in this direction exceeds the microscopically small size of the simulation cell [47]. To obtain reliable estimates for  $\kappa_{yy}$  in the thermodynamic limit ( $s_y \rightarrow \infty$ ) (which are plotted in Fig. 4), we applied a finite-size scaling analysis detailed in Ref. [33]. The observed system-size dependence suggests that in the vicinity of the peak of  $\kappa_{yy}$  ( $c_r = \frac{4}{10}$ ) the thermodynamic state of the confined fluid is close to a critical point. However, we defer a discussion of the nature of this critical point to Sec. III D, where we analyze the phase behavior of a closely related lattice-gas model. It is furthermore worthwhile to stress that for the system sizes employed here none of the properties studied depends sensibly on the size of the simulation cell in the  $y$  direction as far as thermodynamic states sufficiently off any critical point are concerned.

On either side of the cusplike peak  $\kappa_{yy}$  decays rapidly to rather small values typical of dense LJ(12,6) fluids. For  $s_z \lesssim 5.5$ ,  $\kappa_{yy}$  oscillates with a period of about one reflecting stratification (see also Fig. 3) [44]. In addition, to its cusplike maximum  $\kappa_{yy}$  also changes discontinuously during the first-order phase transition at  $s_z \approx 8.3$  ( $c_r = \frac{4}{10}$ ). For all  $s_z > 8.3$  the magnitude of  $\kappa_{yy}$  corresponds to a typical LJ(12,6) gas in accord with the plot of  $\bar{\rho}$  in Fig. 3. Stratification-induced oscillations of  $\kappa_{yy}$  can also be seen for  $c_r = \frac{4}{7}$  and small  $s_z$  in Fig. 4. However, in this case  $\kappa_{yy}$  remains rather small up to the substrate separation at which the transition to a gaslike phase occurs ( $s_z \approx 11.0$ ). The smaller value of  $\kappa_{yy}$  ( $c_r = \frac{4}{7}$ ) compared with  $c_r = \frac{4}{10}$  indicates the presence of a denser fluid. This seems sensible because the net attraction of fluid molecules by the substrate is larger for  $c_r = \frac{4}{7}$  than for  $c_r = \frac{4}{10}$ .

### III. MEAN-FIELD THEORY

To understand the effect of chemical corrugation of the substrate on the phase behavior of a confined fluid, one needs

to know its phase diagram as a function of  $s_z$  and  $c_r$ . In terms of computer time it is rather tedious to compute the phase diagram by GCEMC for the model introduced in Sec. II. Instead we employ a mean-field lattice-gas model with nearest-neighbor (square-well) interactions between molecules on a simple cubic lattice which reduces the computational burden substantially, thereby permitting a more detailed study of the phase behavior of fluids confined between chemically corrugated substrates. This also enables a qualitative understanding of results obtained for the more realistic model discussed in Sec. II.

#### A. Lattice gas

At the mean-field level, the free energy of the lattice gas can be written as [35,48]

$$F[\rho(\mathbf{r})] = \sum_{\mathbf{r}} \left\{ k_B T [\rho(\mathbf{r}) \ln \rho(\mathbf{r}) + [1 - \rho(\mathbf{r})] \times \ln [1 - \rho(\mathbf{r})]] - \frac{\epsilon_{ff}}{2} \sum_{\mathbf{r}'} \rho(\mathbf{r}) \rho(\mathbf{r}') \right\}, \quad (18)$$

which is a functional of the local density  $0 \leq \rho(\mathbf{r}) \leq 1$  (in units of  $\ell$ ) at lattice site,  $\mathbf{r}$ . At each lattice site,  $\rho(\mathbf{r})$  may vary continuously between the limits stated. In the third term on the right side of Eq. (18), which accounts for interactions between lattice-gas molecules, we restrict the summation to nearest neighbors of site  $\mathbf{r}$  (indicated by the prime on the summation sign), and  $\epsilon_{ff}$  determines the strength of the interaction (see Fig. 5). For the mean-field Ising model of a magnet, which is intimately related to the mean-field lattice gas (see, for instance, Sec. 1.9 in Ref. [48]), Baxter [48] pointed out that the Hamiltonian is unphysical because the interaction strength depends on the number of spins. In addition, Eq. (18) obviously ignores intermolecular correlations so that a correct description of critical phenomena is prevented. Nevertheless, as pointed out by Röcken and Tarazona [35], a qualitatively satisfactory picture of first-order phase transitions away from the critical point is provided by the present treatment.

To compute the phase diagram of the lattice gas, we seek minima of the grand potential [49,50]:

$$\Omega[\rho(\mathbf{r})] = F[\rho(\mathbf{r})] + \sum_{\mathbf{r}} [\Phi(\mathbf{r}; s_x, s_z) - \mu] \rho(\mathbf{r}). \quad (19)$$

In Eq. (19),

$$\Phi(\mathbf{r}; s_x, s_z) = \begin{cases} \infty, & |z|/\ell < s_z/2\ell \\ -\epsilon_{fs}, & |x|/\ell < d_s/2\ell \\ -\epsilon_{fw}, & |x|/\ell > d_s/2\ell \end{cases}, \quad |z|/\ell = s_z/2\ell \\ 0, \quad |z|/\ell > s_z/2\ell \quad (20)$$

describes the (square-well) interaction between lattice-gas molecules and the substrate similar to the fluid-substrate interaction potential employed in the parallel computer simulations [see Eqs. (2)–(6) and Figs. 1 and 5].

From the functional derivative of Eq. (19) we obtain the Euler-Lagrange equation

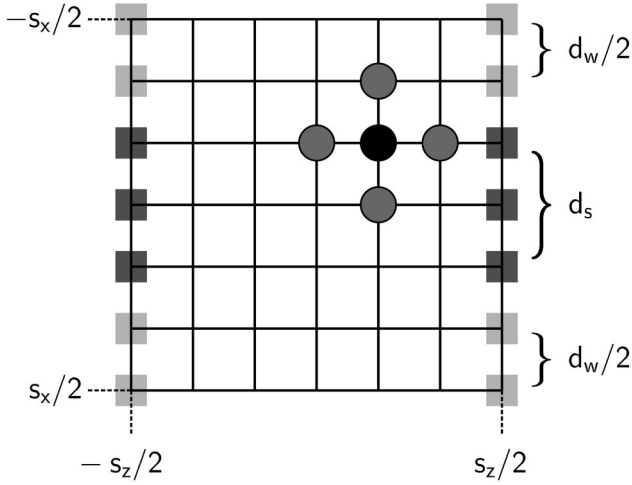


FIG. 5. Scheme of the lattice-gas model of a fluid confined between chemically corrugated substrates in the  $x$ - $z$  plane. The coordinate system is centered at the point  $(0,0)$  halfway between the substrates located at  $\pm s_z/2$ . Each molecule (black circle) interacts with its nearest neighbors (grey circles). The two remaining nearest neighbors on the simple-cubic lattice located at lattice sites in the translationally invariant  $y$  direction perpendicular to the paper plane are not shown. Sites at which a lattice-gas molecule is subject to the substrate interaction  $\Phi(\mathbf{r}; s_x, s_z) = -\epsilon_{fs}$  are shaded in dark grey (strongly attractive substrate portions, width  $d_s$ ), whereas sites at which  $\Phi(\mathbf{r}; s_x, s_z) = -\epsilon_{fw}$  (weakly attractive substrate portions, width  $d_w$ ) are shaded in lighter grey [see Eq. 20]. In the  $x$  direction, periodic boundary conditions are applied (see text).

$$0 = \frac{\delta\Omega}{\delta\rho(\mathbf{r})} = \epsilon_{ff} \sum_{\mathbf{r}'} \rho(\mathbf{r}') - k_B T \ln \left[ \frac{\rho(\mathbf{r})}{1-\rho(\mathbf{r})} \right] + \mu - \Phi(\mathbf{r}) \quad (21)$$

which we solve numerically for its zeros (see Sec. III B). Considering as a special case the bulk lattice gas, the density becomes nonlocal because the symmetry-breaking substrate potential vanishes identically, and Eq. (21) simplifies to

$$f_{i,j} := \tilde{\rho}_{i,j} - \tanh \left\{ \frac{1}{2k_B T} \left[ \hat{\mu} - \Phi_{i,j} + \frac{\epsilon_{ff}}{2} (2\tilde{\rho}_{i,j} + \tilde{\rho}_{i-1,j} + \tilde{\rho}_{i+1,j} + \tilde{\rho}_{i,j-1} + \tilde{\rho}_{i,j+1}) \right] \right\} = 0, \quad (25)$$

where  $\hat{\mu} := \mu + 3\epsilon_{ff}$ ,  $\tilde{\rho}_{i,j} \equiv \tilde{\rho}(x_i, z_j; s_x, s_z)$ ,  $\Phi_{i,j} \equiv \Phi(x_i, z_j; s_x, s_z)$ , and the sum over nearest-neighbor interactions in Eq. (24) has been written explicitly based upon the cubic symmetry of the lattice and its translational invariance in the  $y$  direction. Equation (25) is similar to Eq. (4) of the work by Bruno, Marini Bettolo Marconi, and Evans, who considered a mean-field lattice gas interacting with a chemically homogeneous substrate [50]. In the  $x$  direction we employ periodic boundary conditions, that is,  $\tilde{\rho}_{n_x+1,j} = \tilde{\rho}_{1,j}$ ,  $\tilde{\rho}_{0,j} = \tilde{\rho}_{n_x,j}$ . Because of Eq. (20),  $\tilde{\rho}_{i,0} = \tilde{\rho}_{i,n_z+1} = 0$  [for the bulk lattice gas  $\Phi(\mathbf{r}; s_x, s_z) = 0 \forall \mathbf{r}$  and periodic boundary conditions are invoked in the  $z$  direction as well]. To proceed, it is also convenient to employ a single index by introducing the transformation  $i, j \rightarrow k = (i-1)n_z + j$  ( $i = 1, \dots, n_x$ ;  $j = 1, \dots, n_z$ ), so that the set of functions  $\{f_{i,j}\}$  and local “magnetizations”  $\{\tilde{\rho}_{i,j}\}$  can be treated as  $k_{\max}$ -dimensional vectors  $\mathbf{f} := (f_1, f_2, \dots, f_{k_{\max}})$  and  $\tilde{\boldsymbol{\rho}} := (\tilde{\rho}_1, \tilde{\rho}_2, \dots, \tilde{\rho}_{k_{\max}})$  where  $k_{\max} := n_x n_z$ . In vector notation Eq. (25) then becomes

$$\mathbf{f}(\tilde{\boldsymbol{\rho}}) = \mathbf{0}. \quad (26)$$

Suppose a suitable initial guess  $\tilde{\boldsymbol{\rho}}^{[0]}$  for the magnetization vector exists (see Sec. III C). One may then expand  $\mathbf{f}$  in a Taylor series as

$$6\epsilon_{ff}\rho - k_B T \ln \left[ \frac{\rho}{1-\rho} \right] + \mu = 0, \quad (22)$$

where the factor of 6 arises on account of the assumed cubic symmetry of the lattice. To proceed it is advantageous to employ the close relationship with the Ising model and introduce a “magnetization”  $-1 \leq \tilde{\rho}(\mathbf{r}) \leq 1$  via

$$\rho(\mathbf{r}) = \frac{1}{2} [1 + \tilde{\rho}(\mathbf{r})]. \quad (23)$$

In this “magnetic” language, Eq. (21) can be recast as

$$\tilde{\rho}(\mathbf{r}) = \tanh \left\{ \frac{1}{2k_B T} \left[ \mu - \Phi(\mathbf{r}; s_x, s_z) + \frac{\epsilon_{ff}}{2} \sum_{\mathbf{r}'} [1 + \tilde{\rho}(\mathbf{r}')] \right] \right\}. \quad (24)$$

For the bulk lattice gas a similar expression can be obtained from Eq. (22), from which one can verify analytically [48] that in units of  $\epsilon_{ff}$  and  $\ell$ , in which we shall express all quantities henceforth, the bulk critical temperature  $T_{cb} = \frac{3}{2}$ , the critical density  $\rho_{cb} = \frac{1}{2}$ , and the chemical potential at the critical point  $\mu_{cb} = -3$ . Furthermore, as  $T \rightarrow T_{cb}^-$  the shape of the coexistence curve  $\Delta\rho_{\text{coex}}^l := \rho_{\text{coex}}^l - \rho_{\text{coex}}^g \propto (T_{cb} - T)^\beta$  where  $\rho_{\text{coex}}^l$  and  $\rho_{\text{coex}}^g$  are the densities of coexisting bulk liquid and gas phases, respectively, and the critical exponent  $\beta = \frac{1}{2}$ , as it must for a mean-field theory [48].

## B. Numerical solution of the Euler-Lagrange equation

Because of the symmetry of  $\Phi(\mathbf{r}; s_x, s_z) \equiv \Phi(x, z; s_x, s_z)$  [see Eq. (20)] the local density is a function of  $x$  and  $z$ . Thus Eq. (24) needs to be solved for each site on a square lattice of  $n_x \times n_z$  sites, where the integers  $n_x := s_x/\ell$  and  $n_z := s_z/\ell$  reflect the geometry of the model. Numerically, this requires a solution of  $n_x \times n_z$  coupled algebraic equations of the form [see Eq. (24)]

$$\mathbf{f}(\tilde{\boldsymbol{\rho}}) = \mathbf{f}(\tilde{\boldsymbol{\rho}}^{[0]}) + \underbrace{\frac{\partial (f_1, f_2, \dots, f_{k_{\max}})}{\partial (\tilde{\rho}_1, \tilde{\rho}_2, \dots, \tilde{\rho}_{k_{\max}})} \bigg|_{\tilde{\boldsymbol{\rho}}^{[0]}}}_{\mathbf{A}(\tilde{\boldsymbol{\rho}}^{[0]})} \cdot (\tilde{\boldsymbol{\rho}} - \tilde{\boldsymbol{\rho}}^{[0]}) + \dots = \mathbf{0}, \quad (27)$$

where the Jacobian matrix (of  $k_{\max} \times k_{\max}$  elements)  $\mathbf{A}(\tilde{\boldsymbol{\rho}}^{[0]})$  is evaluated for the initial solution  $\tilde{\boldsymbol{\rho}}^{[0]}$ . Its elements  $A_{m,n} = 0$  ( $m = 1, \dots, k_{\max}; n = 1, \dots, k_{\max}$ ) if  $m \neq n$  and lattice site  $n$  is not a nearest neighbor of  $m$ . If either one of these conditions does not apply one verifies easily from Eq. (25) that

$$A_{m,n} = \begin{cases} 1 - \frac{\epsilon_{ff}}{2k_B T} \left( 1 - \tanh^2 \left[ \left( \hat{\mu} - \Phi_k + (\epsilon_{ff}/2) \sum_{k'} \tilde{\rho}_{k'} \right) / 2k_B T \right] \right), & m = n, \\ -\frac{\epsilon_{ff}}{4k_B T} \left( 1 - \tanh^2 \left[ \left( \hat{\mu} - \Phi_k + (\epsilon_{ff}/2) \sum_{k'} \tilde{\rho}_{k'} \right) / 2k_B T \right] \right), & m \neq n. \end{cases} \quad (28)$$

Neglecting in Eq. (27) higher than linear terms in  $\tilde{\boldsymbol{\rho}} - \tilde{\boldsymbol{\rho}}^{[0]}$  gives a linear equation

$$\tilde{\boldsymbol{\rho}}^{[k+1]} = \tilde{\boldsymbol{\rho}}^{[k]} - \mathbf{A}^{-1}(\tilde{\boldsymbol{\rho}}^{[k]}) \cdot \mathbf{f}(\tilde{\boldsymbol{\rho}}^{[k]}) \quad (29)$$

for the magnetization vector, which we solve iteratively in the following steps: (1) Compute matrix  $\mathbf{A}$  [see Eq. (28)] and vector  $\mathbf{f}$  [see Eq. (25)] for the initial magnetization vector  $\tilde{\boldsymbol{\rho}}^{[0]}$ . (2) Compute the inverse matrix  $\mathbf{A}^{-1}$  by Gauß elimination. (3) Solve Eq. (29) for  $\tilde{\boldsymbol{\rho}}^{[1]}$ , replace  $\tilde{\boldsymbol{\rho}}^{[0]}$  by  $\tilde{\boldsymbol{\rho}}^{[1]}$ , and return to step 1. This algorithm, known as the method of Newton-Kantorowitsch [51], is halted when  $\max |\tilde{\rho}^{[l+1]} - \tilde{\rho}^{[l]}| \leq 10^{-7}$  which is generally achieved in 4–6 iterations (see Sec. III C).

### C. Phase diagrams

For temperatures below the critical temperature, several solutions of Eq. (26) may exist. For the bulk lattice gas, which we chose to test our implementation of the Newton-Kantorowitsch method, only homogeneous gas and liquid phases coexist. The thermodynamically stable phase is the one minimizing the grand potential [see Eq. (19)] (where, of course, in the bulk  $\Phi(\mathbf{r}; s_x, s_z) \equiv 0 \forall \mathbf{r}$ ). To find the thermodynamically stable phase, suitable initial magnetization vectors  $\tilde{\boldsymbol{\rho}}^{[0]}$  are required. These can be constructed by realizing that for  $T \leq T_{cb}$  and  $\mu$  sufficiently below  $\mu_{cb}$  a gas phase will be thermodynamically stable, whereas, on the other hand, this phase will be a liquid if  $\mu$  exceeds  $\mu_{cb}$  sufficiently. Thus, as initial solutions of Eq. (29), we take

$$\tilde{\boldsymbol{\rho}}^{[0]} = \begin{cases} \mathbf{0}, & \mu < \mu_{cb} \\ \mathbf{1}, & \mu > \mu_{cb}, \end{cases} \quad (30)$$

where  $\mathbf{0}$  and  $\mathbf{1}$  are vectors of  $k_{\max}$  elements all set to 0 or 1, respectively. Our numerical procedure then involves the following steps.

- (1) Choose an initial temperature  $T_k < T_{cb}$ .
- (2) Choose a chemical potential  $\mu_{k'}$  sufficiently below (above)  $\mu_{cb}$ .

(3) Solve Eq. (29) under these conditions iteratively to obtain a solution vector with  $k_{\max}$  elements all equal to the homogeneous gas (liquid) density  $\rho_{k'}^g < \rho_{cb}$  ( $\rho_{k'}^l > \rho_{cb}$ ).

(4) Compute  $\Omega_{k'}^g, (\Omega_{k'}^l)$  [see Eqs. (18) and (19)] with the final magnetization vector  $\tilde{\boldsymbol{\rho}}_{k'}$  from Eq. (29).

(5) As long as a solution of Eq. (29) is obtained numerically (see below), set  $\mu_{k'+1} = \mu_{k'} + \Delta\mu$ ,  $\mu_{k'} < \mu_{cb}$  ( $\mu_{k'+1} = \mu_{k'} - \Delta\mu$ ,  $\mu_{k'} > \mu_{cb}$ ), replace  $\mu_{k'}$  by  $\mu_{k'+1}$ , and return to step 3; if no solution of Eq. (29) is obtained numerically, set  $T_{k+1} = T_k + \Delta T$ , replace  $T_k$  by  $T_{k+1}$ , and return to step 1 until  $T_{k+1} = T_{cb}$ .

For a successful implementation of the iterative procedure described in Sec. III B, it is important to realize that for the bulk lattice gas the curve  $\mu = \mu(\rho_b)$  and  $T < T_{cb}$  has the usual S-shaped form (i.e., a van der Waals loop) with a maximum at some  $\mu_{\max} > \mu_{cb}$  and a minimum at some other  $\mu_{\min} < \mu_{cb}$ , where the corresponding densities  $\rho(\mu_{\min}) > \rho(\mu_{\max})$  (see Fig. 6). Thus an intermediate range of chemical potentials exists such that Eq. (29) has three solutions for a given  $T$  and  $\mu$ . That is, for the same  $T$  and  $\mu$ ,  $\rho(\mu)$  can

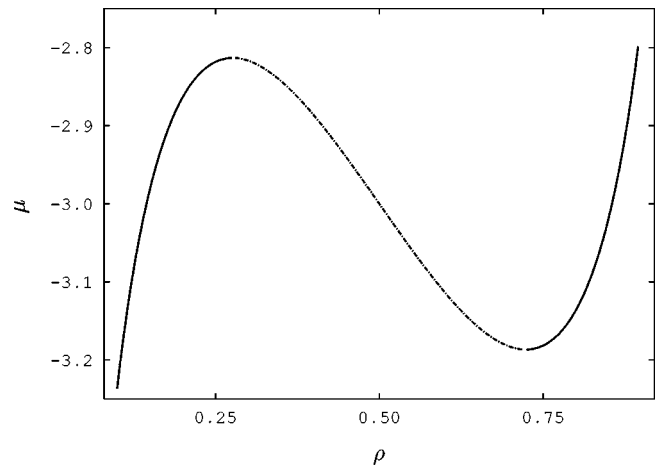


FIG. 6. van der Waals loop in a plot of  $\mu = \mu(\rho)$  for the bulk mean-field lattice gas for  $T/T_{cb} = 0.8$ . The Newton-Kantorowitsch algorithm yields solutions of Eq. (22) only in regions represented by (—); in regions represented by (---), the algorithm is numerically unstable (see Sec. III B).

have three different values [coinciding only at the critical point  $(T_{cb}, \mu_{cb})$ ]; outside this range  $\mu = \mu(\rho)$  is a unique function of  $\rho$  (see Fig. 6). In practice, and depending on the preparation of the initial solution [see Eq. (30)] a solution of Eq. (26) is obtained only up to  $\mu_{\max}$  coming from the gas side or down to  $\mu_{\min}$  coming from the liquid side, respectively. Over the range  $\rho(\mu_{\max}) < \rho < \rho(\mu_{\min})$  the iterative procedure becomes unstable, as reflected by a dramatic increase in the number of iterations required to solve Eq. (26). The onset of this numerical instability is very sharp: as  $\mu \rightarrow \mu_{\max}^-$  ( $\mu \rightarrow \mu_{\min}^+$ ) 4–6 iterations suffice to solve Eq. (26), whereas a rapid increase in the number of iterations required by one or two orders of magnitude are observed in the immediate vicinity of the threshold values  $\mu_{\max}$  and  $\mu_{\min}$ . If  $\mu_{\max} - \mu < 10^{-4}$  ( $\mu - \mu_{\min} < 10^{-4}$ ), convergence of the Newton-Kantorowitsch method is not achieved according to the criterion given in Sec. III B. Thus the Newton-Kantorowitsch method as implemented here permits access to only two solutions of Eq. (26). These correspond to minima of the grand potential; the third one [corresponding to a maximum of  $\Omega$ , and hence to a thermodynamically unstable solution of Eq. (26)] turns out to be numerically inaccessible in practice. Fortunately, this solution is irrelevant in the present context.

Since the grand potentials  $\Omega^g$  and  $\Omega^l$  are available for all the solutions  $\rho^g \equiv \rho(\mu < \mu_{\max})$  and  $\rho^l \equiv \rho(\mu > \mu_{\min})$  the densities  $\rho_{\text{coex}}^g$  and  $\rho_{\text{coex}}^l$  can easily be obtained from the intersection of the curves  $\Omega^g = \Omega^g(\mu)$  and  $\Omega^l = \Omega^l(\mu)$  at a point  $(\Omega^{gl}, \mu^{gl})$  (fixed  $T = T_{\text{coex}}$ ). Densities of the coexisting gas and liquid phases at this temperature are determined by  $\rho_{\text{coex}}^g = \rho^g(\mu^{gl}, T_{\text{coex}})$  and  $\rho_{\text{coex}}^l = \rho^l(\mu^{gl}, T_{\text{coex}})$ . For  $T \geq T_{cb}$ ,  $\Omega^g(\mu)$  and  $\Omega^l(\mu)$  become indistinguishable. A plot of the numerically determined coexistence curve for the bulk lattice gas in Fig. 7(a) shows that  $T_{cb} = \frac{3}{2}$  and  $\rho_{cb} = \frac{1}{2}$ . An analysis of  $\Delta\rho^{gl}$  gives  $\beta = \frac{1}{2}$  in accord with the analytically computed values (see Sec. III A), which demonstrates the reliability of our numerical procedure.

Turning now to a mean-field lattice gas confined by chemically heterogeneous substrates, we realize from the work of Röcken and Tarazona [35] that the phase diagram may become much more complex depending on the degree of chemical corrugation of the substrate (i.e.,  $c_r$ ) and the severity of confinement (i.e.,  $s_z$ ). For example, in addition to (inhomogeneous) gaslike and liquidlike phases occupying the entire volume between the substrates, liquid bridges may occur as a third legitimate phase. However, on account of the mean-field character of the Helmholtz free energy, liquid bridges in the lattice-gas model are not subject to stratification (see, for example, Fig. 2 in Ref. [35]); that is,  $\rho(x, z)$  does not oscillate as function of the distance from the substrate as its counterpart computed in the parallel GCEM simulations (see Fig. 2).

The construction of the phase diagram now becomes more complicated because three curves  $\Omega^g(\mu)$ ,  $\Omega^l(\mu)$ , and  $\Omega^b(\mu)$  for the liquid bridges may obtain. To determine the former two we employed the same procedure as for the bulk lattice gas with initial solutions given by Eq. (30). For the liquid-bridge phases we use [in the original square-lattice notation, see Sec. III B, Eq. (20)]

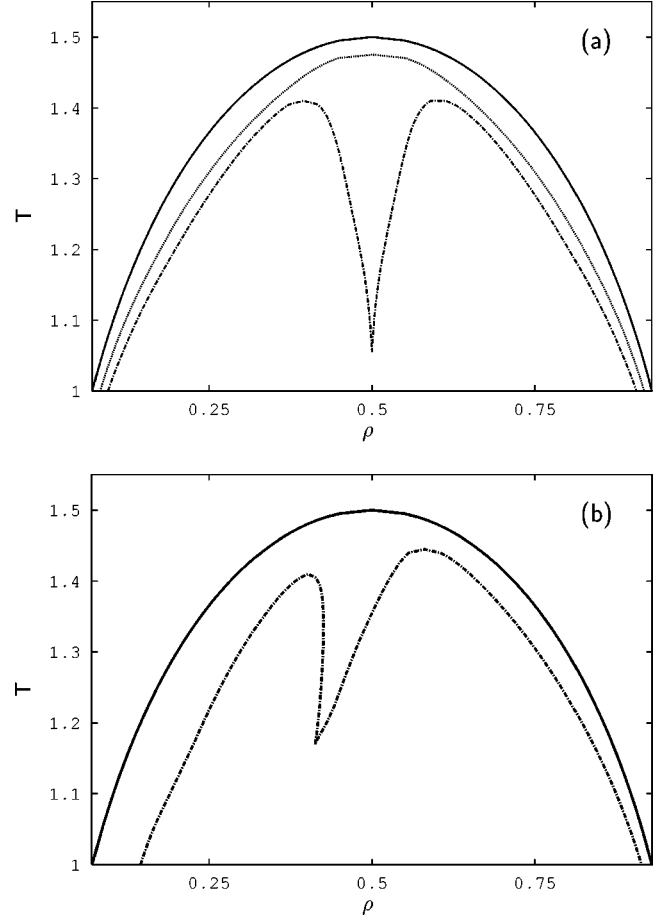


FIG. 7. Coexistence curves for the lattice-gas model. (a) Bulk (—); chemically corrugated substrate ( $n_x=16$ ,  $c_r=0.5$ ,  $\epsilon_{fs}=0.8\epsilon_{fw}=0.2$ )  $n_z=15$  (---),  $n_z=7$  (-·-·). (b) Chemically corrugated substrate characterized by  $n_x=18$ ,  $n_z=9$ ,  $c_r=6/18$ ,  $\epsilon_{fs}=1.4$ , and  $\epsilon_{fw}=0.3$  (-·-·); for comparison, the bulk coexistence curve (—) is also shown.

$$\rho_{i,j}^{[0]} = \begin{cases} 1, & |x|/\ell < d_s/2\ell \\ 0, & |x|/\ell > d_s/2\ell \end{cases} \quad (31)$$

as the initial solution regardless of the  $z$  coordinate of a lattice-gas molecule. For each temperature  $T$  we take  $\mu_{cb}$  as the initial value of the chemical potential. By decreasing, and increasing the chemical potential from its initial value, respectively, we solve Eq. (29) until the algorithm becomes numerically unstable according to the foregoing discussion. With these solutions we construct  $\Omega^b(\mu)$  from Eqs. (18)–(20) and (23). For sufficiently low temperatures two intersections between the curves  $\Omega^b(\mu)$  and  $\Omega^l(\mu)$  at a point  $(\Omega^{bl}, \mu^{bl})$  and between  $\Omega^b(\mu)$  and  $\Omega^g(\mu)$  at another point  $(\Omega^{gb}, \mu^{gb})$  are observed; a third intersection exists at a point  $(\Omega^{gl}, \mu^{gl})$  (see Fig. 8). Because  $\Omega$  is always a monotonically decreasing function of  $\mu$  and because the relation  $(\partial\Omega^g/\partial\mu) \dots > (\partial\Omega^b/\partial\mu) \dots > (\partial\Omega^l/\partial\mu) \dots$  holds for temperatures below the critical temperature(s) (see below) (where “...” is shorthand notation for “all other natural variables of  $\Omega$  fixed”), three different situations are discernible.

(1) For sufficiently low temperatures only (inhomogeneous) gaslike and liquidlike phases coexist; liquid-bridge

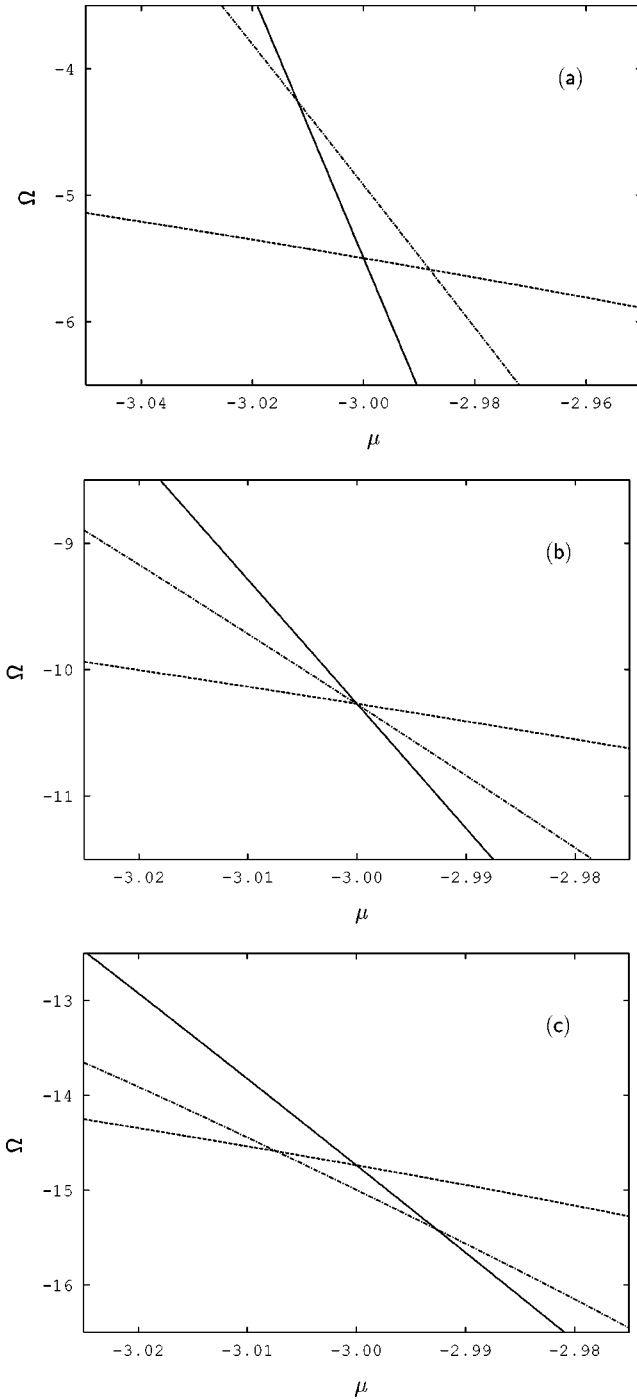


FIG. 8. Grand potential  $\Omega[\rho(r)]$  as a function of chemical potential  $\mu$  [see Eq. (19)] for gaslike (---), liquid bridges (- · -), and liquidlike phases (—). (a)  $T/T_{cb} = 0.6$  ( $T < T_{tr}$ ), (b)  $T/T_{cb} = 0.7$  ( $T = T_{tr}$ ), (c)  $T/T_{cb} = 0.8$  ( $T > T_{tr}$ ). A pair of curves intersects at points  $(\Omega^{gl}, \mu^{gl})$ ,  $(\Omega^{gb}, \mu^{gb})$ , and  $(\Omega^{bl}, \mu^{bl})$ , corresponding to coexistence between thermodynamically stable or metastable phases. The apparent linear dependence of  $\Omega[\rho(r)]$  on  $\mu$  is a result of the expanded scale on both axes.

phases are metastable because of the relations [see Fig. 8(a)]

$$\Omega^{bl} > \Omega^{gl} > \Omega^{gb},$$

$$\mu^{bl} < \mu^{gl} < \mu^{gb}.$$

(2) At  $T = T_{tr}$ , a triple point exists at which all three phases coexist because [see Fig. 8(b)]

$$\Omega^{bl} = \Omega^{gl} = \Omega^{gb},$$

$$\mu^{bl} = \mu^{gl} = \mu^{gb}.$$

(3) Above  $T_{tr}$ , a gaslike phase coexists with a lower-density liquid-bridge phase, and a higher-density liquid-bridge phase coexists with a liquidlike phase since

$$\Omega^{bl} < \Omega^{gl} < \Omega^{gb},$$

$$\mu^{bl} > \mu^{gl} > \mu^{gb}.$$

For all  $T > T_{tr}$ , gaslike and liquidlike phases no longer coexist [see Fig. 8(c)]. Note also that this suggests existence of two critical points  $(T_{cp}^{gb}, \rho_{cp}^{gb})$  and  $(T_{cp}^{bl}, \rho_{cp}^{bl})$  at which the curves of each pair  $[\Omega^g(\mu), \Omega^b(\mu)]$  and  $[\Omega^b(\mu), \Omega^l(\mu)]$  become indistinguishable. This situation is depicted in Figs. 7(a) and 7(b). Because in Fig. 7(a),  $d_s = d_w = 8$ , and because  $\epsilon_{fs} = 0.8$  and  $\epsilon_{fw} = 0.2$  both critical temperatures are the same but significantly lower than  $T_{cb}$ . Compared with the bulk critical density  $\rho_{cb} = \frac{1}{2}$ , the gas-bridge critical densities are shifted to lower ( $\rho_{cp}^{gb} \approx 0.395$ ) and higher values ( $\rho_{cp}^{bl} \approx 0.605$ ), respectively. With respect to  $\rho_{cb}$  this shift is symmetric because of our present choice of  $d_s$ ,  $d_w$ ,  $\epsilon_{fw}$ , and  $\epsilon_{fs}$  [see Fig. 7(a)] [35]. As expected, a triple point is observed at  $\rho_{tr} = \frac{1}{2}$  and  $T_{tr} \approx 1.055$  below the critical temperatures  $T_{cp}^{gb} = T_{cp}^{bl} \approx 1.410$ . For different substrate parameters less symmetric curves obtain, as the plot in Fig. 7(b) shows. Similar effects were observed earlier by Röcken and Tarazona [35], who employed a different model substrate. For a lessened degree of confinement (i.e., as  $s_z$  increases) the chemical heterogeneity of the substrate becomes increasingly insignificant. This can be seen in Fig. 7(a), where the coexistence curve for a  $16 \times 15$  lattice exhibits no triple point and only a single critical point  $T_{cp} \approx 1.475$  and  $\rho_{cp} = \frac{1}{2}$ , which is, however, still lower than  $T_{cb} = \frac{3}{2}$  on account of the prevailing confinement effect.

#### D. Condensation lines

From the phase diagrams discussed in Sec. III C, it is possible to obtain a qualitative picture of the phase behavior of fluids in the more complex model investigated in Sec. II. However, it proves convenient to discuss the phase behavior of the lattice gas in terms of condensation lines  $\mu = \mu(T_{coex})$  rather than the analogous phase diagrams plotted in Fig. 7. For example, the bulk phase diagram displayed in Fig. 7 reduces to a line  $\mu_b(T_{coex}) = -3$  ending at  $T_{coex} \equiv T_{cb} = \frac{3}{2}$  (see Fig. 9). (In the corresponding Ising model for zero magnetic field, this line coincides with the temperature axis [52].) Condensation lines represent lines of first-order phase transitions in thermodynamic state  $(\mu-T)$  space terminating at the critical point(s).

Condensation lines for the lattice gas confined between chemically corrugated substrates are more complex, as the corresponding plots in Fig. 9 illustrate. First, these lines are no longer parallel to the  $T$  axis. Second, they consist of several branches corresponding to coexistence between inhomogeneous gaslike and liquidlike phases, gaslike phases and

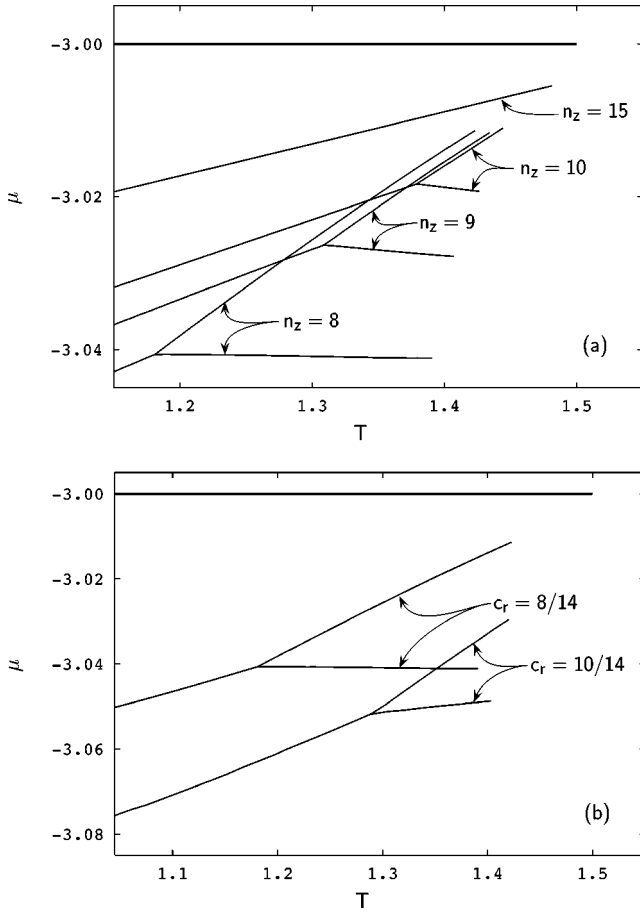


FIG. 9. Pore condensation lines  $\mu = \mu(T_{\text{coex}})$  for various lattice gases. The horizontal line  $\mu(T_{\text{coex}}) = -3$  represents the bulk curve terminating at  $T_{\text{coex}} \equiv T_{cb} = \frac{3}{2}$ . The confined lattice gas is characterized by  $\epsilon_{fs} = 1.4$  and  $\epsilon_{fw} = 0.3$ . In (a), results are shown for various substrate separations  $n_z$  ( $n_x = 14$ ,  $c_r = \frac{8}{14}$ ), whereas in (b) the effect of a varying degree of chemical corrugation of the substrate  $c_r$  is demonstrated for  $n_x = 14$  and  $n_z = 8$ . As for the bulk, condensation lines for the confined lattice gases terminate at the critical point(s) (see text).

liquid bridges, and liquid bridges and liquidlike phases. All three lines intersect at the triple point and branches corresponding to coexistence between gaslike phases and liquid bridges or liquid bridges and liquidlike phases end at the respective critical points (see Fig. 9). One-phase regions corresponding to inhomogeneous gaslike ( $g$ ), liquidlike ( $l$ ), and liquid-bridge phases ( $b$ ) separated by branches of the pore condensation lines are indicated in Fig. 10 for convenience. Third, the location of all three branches with respect to the bulk condensation line depends on the degree of chemical corrugation of the substrate (i.e.,  $c_r$ ) and as well as on the severity of confinement (i.e.,  $s_z$ ). For example, increasing  $s_z$  at constant  $c_r$  causes the triple point to shift to higher temperatures and larger chemical potentials [see Fig. 9(a)]. The critical points approach each other, so that the liquid-bridge one-phase region shrinks. Eventually both critical points coincide with the triple point at sufficiently large  $s_z$ . This case is represented by the plot in Fig. 9(a), corresponding to  $n_z = 15$  [see also Fig. 7(a)]. The resulting pore condensation line is still not parallel to the  $T$  axis, but has no more branches and terminates at a single critical point ( $T_{cp}$

$< T_{cb}$ ,  $\mu_{cp} < \mu_{cb}$ ). In the limit  $s_z \rightarrow \infty$  the condensation line for the confined lattice gas becomes indistinguishable from that of the bulk.

If, on the other hand,  $c_r$  is varied at constant  $s_z$ , condensation lines shift with respect to the bulk condensation line, so that the “distance” from the bulk condensation line increases with  $c_r$ . That is, for more attractive substrates this distance is larger. Variations of  $c_r$  also affect the location of the triple point and the slope of the branches corresponding to coexistence between gaslike phases and liquid bridges and liquid bridges and liquidlike phases, as the plots in Fig. 9(b) show. As a consequence the liquid-bridge one-phase region shrinks with increasing  $c_r$ .

From the plots in Fig. 9, one immediately realizes the complex dependence of the phase behavior of a confined lattice gas on the detailed nature of the chemically heterogeneous substrate. What conclusions can be drawn from this analysis concerning the phase behavior of the related but more complex GCEMC model reflected by the plots of  $\bar{\rho}$  versus  $s_z$  in Fig. 3? Before addressing this question, we need to remind the reader that in the GCEMC simulations of Sec. II the thermodynamic state of the confined fluid was fixed such that a corresponding bulk phase was a gas. Thus, upon varying  $s_z$  at fixed  $c_r$  one expects shifts of the separate branches of the condensation line in a fashion qualitatively similar to the one exhibited in Fig. 9. However, from a physical perspective only the location of the thermodynamic state *relative* to the condensation line matters. Let us therefore construct a “trajectory” of the thermodynamic state in  $\mu$ - $T$  space while holding fixed the location of the condensation line of the confined fluid by fixing  $s_z$  and  $c_r$ . According to the foregoing reasoning, such a trajectory in  $\mu$ - $T$  space is completely equivalent to the varying location of the condensation line with respect to a *fixed* thermodynamic state on which the plots in Fig. 3 are based. However, employing the trajectory is advantageous because it is much easier to visualize than the complex changes of various features of the condensation line upon varying  $s_z$  (see Fig. 9) with respect to a fixed point in thermodynamic state space.

For sufficiently large  $s_z$  the confined fluid in GCEMC is always an inhomogeneous gaslike phase according to the choice of thermodynamic state variables (see Sec. II B). This notion is supported by the plots in Fig. 3, showing that  $\bar{\rho}$  assumes values characteristic of a bulk LJ(12,6) gas for sufficiently large  $s_z$  regardless of  $c_r$ . One therefore knows that starting out at large substrate separations, the trajectory always begins at a point in the one-phase region of gaslike phases (see Fig. 10). Furthermore, from the plots in Fig. 9 it is evident that upon lowering  $s_z$  the entire condensation line moves to lower  $\mu$  and  $T_{tr}$  becomes smaller so that the liquid-bridge one-phase region widens. Consequently, two options exist for an intersection between the trajectory and the condensation line: the characteristic temperature of the intersection may be either above or below  $T_{tr}$ . Both cases are realized in the GCEMC simulations. For example, for  $c_r = \frac{4}{7}$  the plot of  $\bar{\rho}$  exhibits a single discontinuity at  $s_z \approx 11.0$ . A single discontinuity is also observed for  $c_r = \frac{4}{14}$ , but at a distinctly smaller substrate separations  $s_z \approx 8.1$ . An inspection of  $\rho(x, z)$  in the immediate vicinity of the phase transition reveals that the inhomogeneous gaslike phase condenses to an

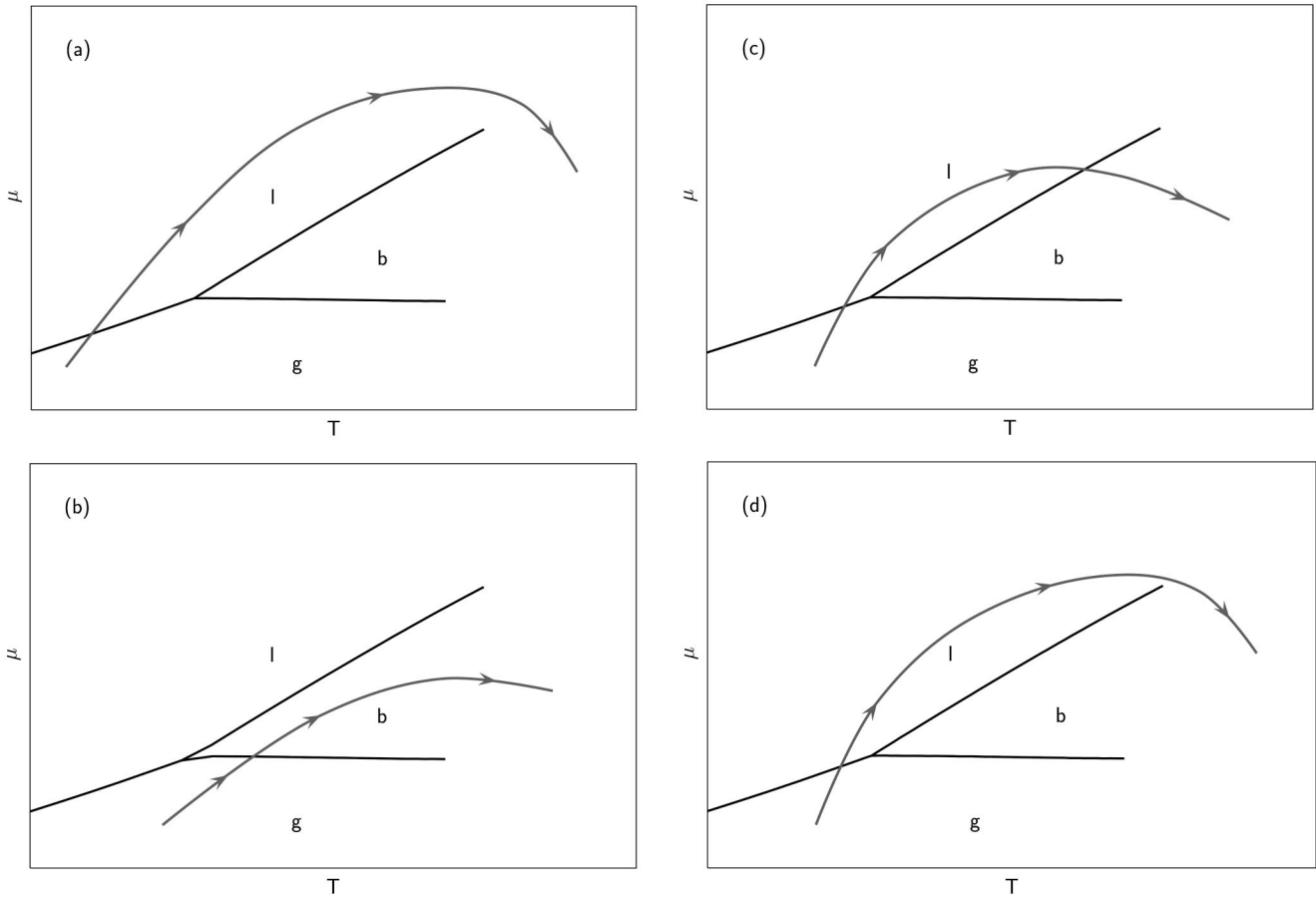


FIG. 10. Scheme of the trajectory in thermodynamic state space (see text) for the various scenarios displayed in Fig. 3. Starting out from a state in the one-phase regime of inhomogeneous gaslike phases, the direction in which the trajectory traverses  $\mu$ - $T$  space is based upon variations of condensation lines displayed in Figs. 9 for decreasing  $n_z$  (i.e.,  $s_z$ ). For increasing  $n_z$  (i.e.,  $s_z$ ), the path in  $\mu$ - $T$  space should be reversed.

inhomogeneous liquidlike phase for  $c_r = \frac{4}{7}$ , whereas the same process leads to a liquid bridge for  $c_r = \frac{4}{14}$ . Thus the trajectory must follow different paths schematically depicted in Figs. 10(a) ( $c_r = \frac{4}{7}$ ) and 10(b) ( $c_r = \frac{4}{14}$ ). From this analysis it follows that the first-order phase transitions occur below ( $c_r = \frac{4}{7}$ ) and above ( $c_r = \frac{4}{14}$ ) the respective triple-point temperatures. The absence of an additional phase transition can be rationalized as follows. For larger  $c_r$  the liquid-bridge one-phase region is narrower (or may be completely absent), and the branch of the condensation line referring to coexistence between gaslike and liquidlike phases ( $T < T_{lr}$ ) is shifted to smaller  $\mu$  [see Fig. 9(b)]. Decreasing  $s_z$  enhances this shift [see Fig. 9(a)]. Both effects favor a single transition from a gaslike phase to a liquidlike phase upon lowering  $s_z$  as observed for  $c_r = \frac{4}{7}$  in Fig. 3. For the overall less attractive substrate  $c_r = \frac{4}{14}$ , this logic implies that after the transition from a gaslike phase to a liquid bridge one stays in the liquid-bridge one-phase region because it widens substantially with decreasing  $s_z$ , as the plots in Fig. 9(a) show. At the same time one expects this transition to occur at smaller  $s_z$ , because the plots in Fig. 9(b) reveal that condensation lines are shifted closer to the bulk condensation line with decreasing  $c_r$ . This is confirmed by Fig. 3.

Because the triple point moves to lower  $T$  and  $\mu$  as  $s_z$  decreases, it is also conceivable that two instead of one first-order transitions occur. This was, in fact, observed for  $c_r$

$= \frac{4}{12}$  in Fig. 3. The first of these is similar to the one for  $c_r = \frac{4}{7}$ ; that is, an inhomogeneous gaslike phase condenses to a liquidlike one. This transition occurs at a temperature *lower* than  $T_{lr}$  for this particular  $s_z$ . However, since  $T_{lr}$  becomes smaller with decreasing  $s_z$ , a second transition may occur during which the inhomogeneous liquidlike phase is transformed into a liquid bridge. This transition occurs *above* the relevant triple-point temperature, and the trajectory follows the path indicated in Fig. 10(c). An inspection of  $\rho(x, z)$  in the vicinity of both phase transitions confirms this notion.

A particularly interesting situation arises for  $c_r = \frac{4}{10}$ , where the inhomogeneous gaslike phase first condenses to a liquidlike phase at  $s_z \approx 8.3$  (see Fig. 3). Over the range  $5.5 \lesssim s_z \lesssim 6.5$  the plot of  $\bar{\rho}(s_z)$  exhibits a large positive slope, which is expected if one assumes that the trajectory in thermodynamic state space follows the path indicated in Fig. 10(d). This path implies that the strong variation of  $\bar{\rho}(s_z)$  over the range of substrate separations indicated reflects the proximity to the critical point at which liquidlike phases and liquid bridges become indistinguishable (see Sec. II B 2). This notion is supported by the plot of  $\kappa_{yy}$  in Fig. 4. Since the critical point is not a point on the trajectory in  $\mu$ - $T$  space, the height of the peak of  $\kappa_{yy}$  must be finite in accord with earlier conjectures for the same situation [33]. Since no second phase transition is observed for  $c_r = \frac{4}{10}$  in Fig. 3, we

conclude that the confined fluid remains supercritical with respect to this critical point for all smaller substrate separations [see Fig. 10(d)].

#### IV. CONCLUDING REMARKS

In this paper we investigated the phase behavior of LJ(12,6) fluids confined between chemically heterogeneous substrates forming a slit-shaped nanopore. The substrate is modeled as a periodic sequence of strongly adsorbing slabs (of width  $d_s$ ) alternating with weakly adsorbing ones (of width  $d_w$ ) (see Fig. 1). The model therefore mimics materials that can nowadays be fabricated in the laboratory [6–11]. The thermodynamic state of the fluid is characterized by the (dimensionless) variables  $T$ ,  $\mu$ ,  $s_z$ ,  $d_s$ ,  $d_w$ ,  $\epsilon_{fs}$ , and  $\epsilon_{fw}$ . We fixed  $T=1.00$ ,  $\mu=-11.50$ ,  $d_s=4.00$ ,  $\epsilon_{fs}=1.25$ , and  $\epsilon_{fw}=0.001$ , and examined the dependence of the mean fluid density and isothermal compressibility on  $s_z$  and  $d_w$  (i.e.,  $c_r$ ). By varying  $c_r$  the fluid is exposed to an overall weaker fluid-substrate potential field the smaller  $c_r$  is for a given value of  $s_z$ . To analyze the dependence of the mean density and, in particular, the striking variation of the isothermal compressibility of the fluid further for a certain substrate corrugation, we employ a mean-field lattice-gas model (see Fig. 5), which allows us to determine the phase diagram by solving numerically an Euler-Lagrange equation for the location of minima of the grand potential functional in thermodynamic state space. The phase behavior of the lattice gas can be summarized as follows

(1) For small substrate separations and  $0 < c_r < 1$ , the coexistence curve of the confined lattice gas exhibits a triple point at a temperature  $T_{tr}$ , where an inhomogeneous gas- and liquidlike phase coexist with a liquid bridge. For  $T > T_{tr}$  gaslike and liquidlike phases coexist independently with liquid bridges of different mean densities (i.e., for  $T > T_{tr}$  a one-phase region exists for liquid bridges). Coexistence between gaslike phases and liquid bridges as well as between liquid bridges and liquidlike phases terminates at critical points whose location depend on  $c_r$ ,  $s_z$ , and the strength of the fluid-substrate interaction with both portions of the heterogeneous substrate [see Figs. 7(a) and 7(b)].

(a) For fixed  $s_z$  and  $c_r = \frac{1}{2}$  the triple-point density  $\rho_{tr} = \rho_{cb}$ . Compared with  $\rho_{cb}$  the critical densities of the confined lattice gas are shifted symmetrically to higher and lower values, respectively [see Fig. 7(a)].

(b) Away from  $c_r = \frac{1}{2}$ , the phase diagram is less symmetric in that  $\rho_{tr} \neq \rho_{cb}$  and  $T_{cp}^{gb} \neq T_{cp}^{bl}$ , both of which are smaller than  $T_{cb}$  [see Fig. 7(b)].

(c) Regardless of  $c_r$ ,  $T_{tr}$  increases with  $s_z$  and eventually merges with both critical points for a sufficiently large substrate separation [see Fig. 8(a)], so that the phase diagram exhibits a single critical point at a temperature  $T_{cp} < T_{cb}$  [see Fig. 7(a)] irrespective of  $c_r$ .

(2) Based upon the phase diagrams, pore condensation lines can be constructed. Their form and proximity to the bulk condensation line  $\mu_b = \mu_b(T_{coex}) = -3$  depends on  $c_r$  and  $s_z$  (see Figs. 9).

(3) The shift of the pore condensation lines with respect to the (fixed) bulk coexistence curve enables us to construct trajectories of the thermodynamic state in  $\mu$ - $T$  space relative to the pore condensation lines (see Fig. 10), from which a

qualitative interpretation of the computer simulation results emerges (see Fig. 3).

(4) The cusp in the plot of  $\kappa_{yy}$  versus  $s_z$  ( $c_r = \frac{4}{10}$ ) (see Fig. 4), and the corresponding large slope of  $\rho(s_z)$  (see Fig. 3), which were observed originally in Ref. [33], can now be interpreted as signatures of the approach of the critical point associated with coexisting liquid bridges and liquidlike phases of the confined fluid.

The rather complex phase behavior of a fluid confined between chemically corrugated substrates is a direct consequence of varying  $s_z$  at constant  $T$  and  $\mu$ . These are precisely operating conditions encountered in parallel SFA experiments in which a quantity like  $\bar{\rho}$  can be determined directly by measuring the refractive index of the confined fluid [38]. Therefore, the complex dependence of  $\bar{\rho}$  on both  $s_z$  and  $c_r$  manifest in the plots of Fig. 3 should be accessible in SFA experiments, and may well offer a way of classifying corrugated substrates experimentally.

However, in making contact with laboratory experiments, one may have to consider hysteresis. It is frequently encountered in studies of capillary condensation, where, for example, a pore phase condenses upon *adsorption* at a temperature  $T_{ads}$  whereas it evaporates upon *desorption* at another temperature  $T_{des}$  (see Figs. 1, 3, and 4 in Ref. [18]). Hysteresis refers to the existence of a temperature range  $\Delta T_H := T_{des} - T_{ads} > 0$  over which the excess coverage  $\Gamma$ , which is the key quantity measured, is a double-valued function of  $T$ . From an equilibrium perspective only one of the pore phases, to which the two values of  $\Gamma$  refer, can be thermodynamically stable, that is, correspond to a *global* minimum of  $\Omega$ ; the other one, conforming to a *local* minimum of  $\Omega$ , is metastable.

In a seemingly similar fashion hysteresis has also been observed in GCEMC studies of sorption in chemically homogeneous pores. However, the relation between this hysteresis and the experimental one remains obscure because it was shown in Ref. [53] that in GCEMC hysteresis depends on the size of the simulation cell as well as on the starting configuration in a sensitive and unpredictable way. Thus hysteresis in GCEMC-generated sorption isotherms is caused by nonergodicity of the Markov chain, and should therefore be regarded as an artifact and not as a physical phenomenon.

From a more general perspective existence and lifetime of metastable states are kinetic phenomena intimately linked to the dynamics of the system. In general, Monte Carlo methods do not permit one to study dynamical aspects because they are not based on an equation of motion like, say, Newton's equation. The Metropolis algorithm [39] frequently employed in Monte Carlo simulations is, however, linked to the Chapman-Kolmogoroff equation which describes the temporal evolution of stochastic processes [54]. Thus in specialized cases a dynamical interpretation of the Markov chain generated in the Monte Carlo method is feasible. Perhaps the most prominent such case concerns the dynamics of spin lattices, where even the dynamics in the near-critical regime has been studied successfully in the Monte Carlo method [55]. In Ref. [56] Monte Carlo simulations were employed to investigate intermediate and long-time non-Brownian diffusion in confined monolayer films. Another example concerns the dynamics of the contact line in a model fluid wetting a

disordered substrate [57]. In this latter case, a careful analysis of the simulation data permitted to elucidate aspects of contact-angle hysteresis. However, it must be borne in mind that in every single case the correctness of the dynamical interpretation of Monte Carlo simulations must be established by additional independent (experimental or theoretical) means. A dynamical interpretation of our simulations is beyond the scope of this paper, which is exclusively concerned with phenomena in thermodynamic equilibrium.

## ACKNOWLEDGMENTS

We thank Professor S. Dietrich (Bergische Universität, Wuppertal) for discussions that helped to improve the presentation of the lattice-gas results. We are also grateful to the Sonderforschungsbereich 448 ‘‘Mesoskopisch strukturierte Verbundsysteme’’ for financial support. Computations were carried out on the Cray T94 of the Rechenzentrum at Christian-Albrechts-Universität Kiel.

- 
- [1] T. A. Core, W. K. Tsang, and S. J. Sherman, *Semicond. Sci. Technol.* **36**, 39 (1993).
- [2] J. B. Knight, A. Vishwanath, J. P. Brody, and R. H. Austin, *Phys. Rev. Lett.* **80**, 3863 (1998).
- [3] D. W. L. Tolfree, *Rep. Prog. Phys.* **61**, 313 (1998).
- [4] F. Burmeister, C. Schläfle, B. Keilhofer, C. Bechinger, J. Boneberg, and P. Leiderer, *Adv. Mater.* **10**, 495 (1998).
- [5] P. Bönsch, D. Wüllner, T. Schrimpf, A. Schlachletzki, and R. Lacmann, *J. Electrochem. Soc.* **145**, 1273 (1998).
- [6] A. Kumar and G. M. Whitesides, *Appl. Phys. Lett.* **63**, 2002 (1993).
- [7] J. Drelich, J. D. Miller, A. Kumar, and G. M. Whitesides, *Colloids Surf., A* **93**, 1 (1994).
- [8] J. L. Wilbur, A. Kumar, E. Kim, and G. M. Whitesides, *Adv. Mater.* **6**, 600 (1994).
- [9] R. J. Jackman, J. L. Wilbur, and G. M. Whitesides, *Science* **269**, 664 (1995).
- [10] R. Yang, D. F. Evans, and W. A. Hendrickson, *Langmuir* **11**, 211 (1995).
- [11] P. E. Sheehan and C. M. Lieber, *Science* **272**, 1158 (1996).
- [12] C. Casagrande, P. Fabre, E. Raphaël, and M. Veyssié, *Europhys. Lett.* **9**, 251 (1989).
- [13] P. G. de Gennes, *Rev. Mod. Phys.* **64**, 645 (1991).
- [14] W. Koch, S. Dietrich, and M. Napiórkowski, *Phys. Rev. E* **51**, 3300 (1995).
- [15] S. Dietrich, in *New Approaches to Old and New Problems in Liquid State Theory—Inhomogeneities and Phase Separation in Simple, Complex, and Quantum Fluids held at Patti Marina (Messina), Italy, July 7-17, 1998*, edited by C. Caccamo (Kluwer, Dordrecht, 1998).
- [16] P. Lenz and R. Lipowsky, *Phys. Rev. Lett.* **80**, 1920 (1998).
- [17] W. Gac, A. Patrykiewicz, and S. Sokolowski, *Thin Solid Films* **298**, 22 (1997).
- [18] M. Thommes and G. H. Findenegg, *Langmuir* **10**, 4270 (1994).
- [19] M. Thommes, G. H. Findenegg, and M. Schoen, *Langmuir* **11**, 2137 (1995).
- [20] G. V. Burgess, D. H. Everett, and S. Nutall, *Pure Appl. Chem.* **61**, 1845 (1989).
- [21] A. de Keizer, T. Michalski, and G. H. Findenegg, *Pure Appl. Chem.* **63**, 1495 (1991).
- [22] W. D. Machin, *Langmuir* **10**, 1235 (1994).
- [23] A. P. Y. Wong, S. B. Kim, W. I. Goldburg, and M. H. W. Chan, *Phys. Rev. Lett.* **70**, 954 (1993).
- [24] A. P. Y. Wong and M. H. W. Chan, *Phys. Rev. Lett.* **65**, 2567 (1990).
- [25] R. Evans, in *Liquides aux Interfaces, Les Houches 1988 Session XLVIII, Course 1*, edited by J. Charvolin, J. F. Joanny, and J. Zinn-Justin (North-Holland, Amsterdam, 1990).
- [26] M. Schoen and D. J. Diestler, *J. Chem. Phys.* **109**, 5596 (1998).
- [27] R. Evans, *J. Phys.: Condens. Matter* **2**, 8989 (1990).
- [28] H. Nakanishi and M. E. Fisher, *J. Chem. Phys.* **78**, 3279 (1983).
- [29] M. E. Fisher and H. J. Nakanishi, *J. Chem. Phys.* **75**, 5857 (1981).
- [30] R. Evans, U. Marini Bettolo Marconi, and P. Tarazona, *J. Chem. Soc., Faraday Trans. 2* **82**, 1763 (1986).
- [31] P. Tarazona, U. Marini Bettolo Marconi, and R. Evans, *Mol. Phys.* **60**, 573 (1987).
- [32] Y. K. Tovbin and E. V. Votyakov, *Langmuir* **9**, 2652 (1993).
- [33] M. Schoen and D. J. Diestler, *Phys. Rev. E* **56**, 4427 (1997).
- [34] M. Schoen and D. J. Diestler, *Chem. Phys. Lett.* **270**, 339 (1997).
- [35] P. Röcken and P. Tarazona, *J. Chem. Phys.* **105**, 2034 (1996).
- [36] P. Röcken, A. Somoza, P. Tarazona, and G. H. Findenegg, *J. Chem. Phys.* **108**, 8689 (1998).
- [37] D. J. Diestler, M. Schoen, J. E. Curry, and J. H. Cushman, *J. Chem. Phys.* **100**, 9140 (1994).
- [38] J. Israelachvili, *Intermolecular & Surface Forces*, 2nd ed. (Academic, London, 1992).
- [39] M. P. Allen and D. J. Tildesley, *Computer Simulation of Liquids* (Clarendon, Oxford, 1987).
- [40] M. Plischke and B. Bergersen, *Equilibrium Statistical Physics*, 2nd ed. (World Scientific, Singapore, 1994).
- [41] D. A. McQuarrie, *Statistical Mechanics* (Harper and Row, New York, 1976).
- [42] J. P. Hansen and I. R. McDonald, *Theory of Simple Liquids*, 2nd ed. (Academic, London, 1986).
- [43] R. Balian, *From Microphysics to Macrophysics. Methods and Applications of Statistical Physics* (Springer-Verlag, Heidelberg, 1991), Vol. I.
- [44] M. Schoen, *Ber. Bunsenges. Phys. Chem.* **100**, 1355 (1996).
- [45] M. Schoen, D. J. Diestler, and J. H. Cushman, *J. Chem. Phys.* **100**, 7707 (1994).
- [46] E. Kierlik, M. L. Rosinberg, G. Tarjus, and P. A. Monson, in *Fundamentals of Adsorption 6*, edited by F. Meunier (Elsevier, New York, 1998), p. 867.
- [47] P. G. Watson, in *Phase Transitions and Critical Phenomena*, edited by C. Domb and M. S. Green (Academic, London, 1972), Vol. 2, pp. 150–159.
- [48] R. J. Baxter, *Exactly Solved Models in Statistical Physics* (Academic, London, 1991).
- [49] M. J. de Oliveira and R. B. Griffiths, *Surf. Sci.* **71**, 687 (1978).

- [50] E. Bruno, U. Marini Bettolo Marconi, and R. Evans, *Physica A* **141**, 187 (1987).
- [51] I. N. Bronstein and K. A. Semendjajew, *Taschenbuch der Mathematik*, 21st ed. edited by G. Grosche, V. Ziegler, and D. Ziegler (Deutsch, Frankfurt, 1981), Chap. 7.1.2.4.
- [52] L. E. Reichl, *A Modern Course in Statistical Physics* (University of Texas Press, Austin, 1980).
- [53] M. Schoen, C. L. Rhykerd, Jr., J. H. Cushman, and D. J. Diestler, *Mol. Phys.* **66**, 1171 (1989).
- [54] M. Schoen, in *Computational Methods in Colloid and Interface Science*, edited by M. Borowko (Dekker, New York, 1999).
- [55] M. Krech and D. P. Landau, *J. Phys.: Condens. Matter* (to be published).
- [56] M. Schoen, J. H. Cushman, and D. J. Diestler, *Mol. Phys.* **81**, 475 (1994).
- [57] P. Collet, J. De Coninck, F. Dunlop, and A. Regnard, *Phys. Rev. Lett.* **79**, 3704 (1997).